Integrated Sentinel-1 InSAR and GNSS time-series along the San Andreas fault system

Xiaohua Xu[1], David T. Sandwell[1], Emilie Klein[2] and Yehuda Bock[1].

[1]Institute of Geophysics and Planetary Physics, Scripps Institution of Oceanography, University of California San Diego, La Jolla, CA, USA

[2]Laboratoire de géologie - CNRS UMR 8538, Ecole normale supérieure - PSL University, Paris, France

Abstract

Measuring crustal strain and seismic moment accumulation, is crucial for understanding the growth and distribution of seismic hazards along major fault systems. Here we develop a methodology to integrate 4.5 years (2015 - 2019.5) of Sentinel-1 Interferometric Synthetic Aperture Radar (InSAR) and continuous Global Navigation Satellite System (GNSS) time series to achieve 6 to 12-day sampling of surface displacements at ~500 m spatial resolution over the entire San Andreas fault system (SAFS). We decompose the line-of-sight InSAR displacements into three dimensions by combining the deformation azimuth from a GNSS-derived interseismic fault model. We then construct strain rate maps using a smoothing interpolator with constraints from elasticity. The resulting deformation field reveals a wide array of crustal deformation processes including: on- and off-fault secular and transient tectonic deformation; creep rates on all the major faults; and vertical signals associated with hydrological processes. The strain rate maps show significant off-fault components that were not captured by GNSS-only models. These results are important in assessing the seismic hazard in the region.

Plain Language Summary

Seismic hazard models rely on accurate measurements of small interseismic motion over large space on the Earth's crust. Traditional geodetic models based on Global Navigation Satellite System (GNSS) data cannot resolve small scale deforming patterns, mainly due to expensive and limited station deployment. Interferometric Synthetic Aperture Radar (InSAR) has become the emerging tool for mapping the surface deformation, with its advantages of low-cost and full-coverage. Yet InSAR measurement, compared to GNSS, comes with larger bias from the atmospheric noise, especially over length scales greater than 80 km. Here we combined the two methods to resolve fine spatial scales and achieve high accuracy. Our results are presented as deformation time-series over the entire San Andreas fault system. From these deformation time series we have estimated fault creep rates and strain accumulation. One important finding is that there is significant off-fault strain, though we suspect they are mainly due to hydrological processes. These results will advance our knowledge of the earthquake cycle, strain/moment accumulation, and the associated seismic hazards.

Key points

- A practical approach is developed to integrate Sentinel-1 InSAR and GNSS time-series over the entire San Andreas fault system
- The product is used to estimate fault creep and three components of horizontal crustal strain rate which shows notable off-fault portion
- Challenges remain in splitting tectonic and hydrologic sources and whether hydrologic strain will increase seismic hazards

1. Introduction

An improved understanding of how energy and seismic moment accumulate in the crust and upper mantle along major plate boundaries is essential for forecasting the size and timing of major earthquakes [*Smith-Konter & Sandwell*, 2009; *Field et al.,* 2015; *Weiss et al.,* 2020; *Rollins et al.,* 2020]. Recent studies have shown that most damaging earthquakes occur in areas where the crustal strain rate exceeds 100 nanostrain/yr [e.g., *Elliot et al.*, 2016.; *Zeng et al.*, 2018; *Bayona et al.,* 2021]. Many of these areas are heavily populated and have had major destructive earthquakes. Moreover, one of the largest uncertainties in California earthquake hazard models (i.e., UCERF-3 [*Field et al.*, 2014; *Field et al.*, 2015]) is the amount of plate boundary deformation that is accommodated by off-fault strain and whether this strain is accumulating as elastic or as plastic deformation. Therefore, accurate strain rate measurements are needed to improve earthquake forecasts. Achieving an ideal 100-nanostrain/yr accuracy at a 10-km resolution (i.e., a typical fault locking depth in California) requires a horizontal velocity model that has an accuracy of 1 mm/yr. Moreover, moderate earthquakes, fault creep, and other transient processes produce temporal variations in strain rate that commonly exceed 100-nanostrain/yr [*Holt and Shcherbenko*, 2013; *Klein et al.,* 2019]. Currently continuous GNSS measurements can provide vector deformation better than the required 1 mm/yr accuracy but not with 10 km spatial resolution. InSAR provides very high spatial resolution but cannot achieve the 1 mm/yr accuracy, mainly due to the perturbations from atmospheric noise [*Emardson et al.*, 2003]. In addition, current InSAR systems provide only two components of surface deformation and thus cannot uniquely distinguish between horizontal and vertical strain [*Shen and Liu*, 2020]. Here we develop a path to achieving the time-dependent strain rate mapping objective by combining 4.5 years of measurements from InSAR and GNSS along the San Andreas fault system (SAFS).

The accuracy and spatial resolution of the current strain rate models derived from GNSS velocities can be assessed by comparing results from various groups. An accuracy analysis was performed as part of the developing SCEC Community Geodetic Model (CGM-V1) [*Sandwell et al.,* 2016a]. The 17 models were taken from previous publications [*Zeng & Shen,* 2016; *Shen et al.,* 2015; Smith-*Konter & Sandwell,* 2009; *Tong et al.,* 2014; *Tape et al.,* 2009; *Petersen et al.,* 2008; *Petersen et al.,* 2014; *Platt & Becker,* 2010; *McCaffrey,* 2005; *Loveless & Meade,* 2011; *Hackl et al.,* 2009; *Parsons,* 2006; *Parsons et al.,* 2013; *Kreemer et al.,* 2014; *Flesch et al.,* 2000; *Field et al.*, 2014; *Sandwell & Wessel*, 2016]. The

mean and standard deviation of the 10 "best" well-correlated models is shown in Fig. 1a. Note the standard deviation (Fig. 1b) commonly exceeds 50 nanostrain/yr especially above the major faults where the uncertainties can exceed 100 nanostrain/yr. These significant deviations among the models are not due to inaccuracies in the GNSS data but to the incomplete spatial sampling of the GNSS stations, which is typically 10-20 km in California [*Wei et al.,* 2010].

To further characterize this lack of spatial resolution of the strain rate field, we analyzed the strain rate models by computing cross spectra in their overlapping region in Southern California. Radially-averaged cross spectra were computed between every pair of models using Generic Mapping Tools (GMT) [*Wessel et al.,* 2019]. As illustrated in Fig. 1c, there is a large variation in the coherence between these models. Most models agree well at long wavelengths, but generally disagree at short wavelengths, except those having very similar, or identical, fault models like *Shen et al.* [2015] and *Zeng & Shen* [2016] or *Tong et al.* [2014] and *Smith-Konter & Sandwell* [2009]. The disagreements are due to different physical modeling approaches, assumed fault geometries, and slightly different GNSS velocity data sets. For most pairs, the coherence is high at very long wavelength and decreases to zero coherence at ~10 km. The 0.2 coherence threshold of the median of all the cross spectra is located at 30-40 km wavelengths.

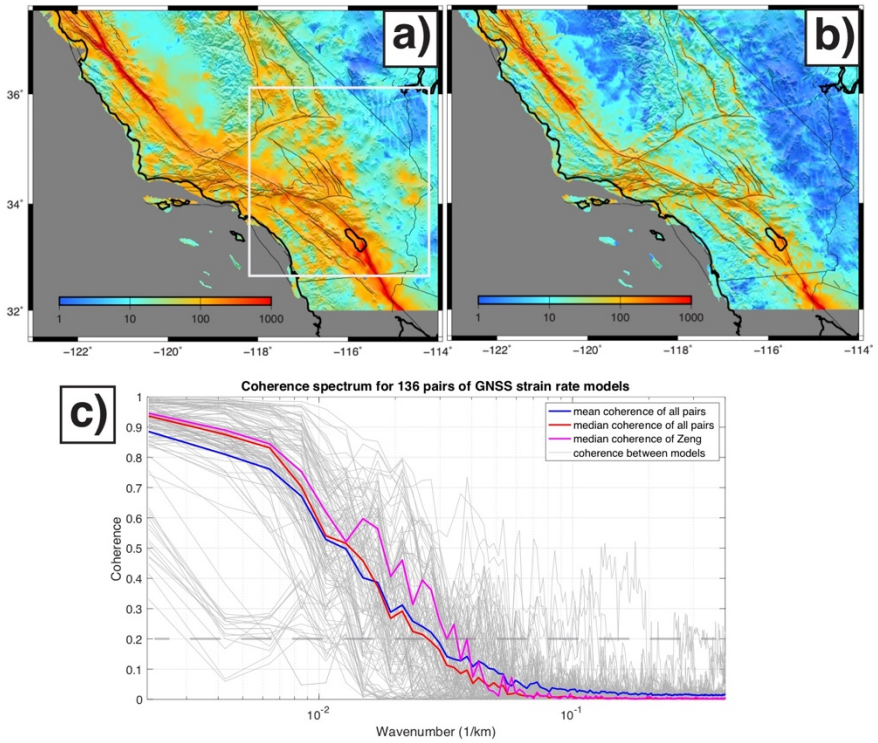

Fig. 1. Second invariant of the horizontal strain rates from GNSS models

[*Sandwell et al.*, 2016a]. a) Average of 10 "best" models based on a spatial correlation analysis. b) Standard deviation of the 10 models. c) Radially-averaged cross spectra between all pairs of SCEC CGM-V1 strain rate models, performed in the area denoted by the white box in a). The mean and median of all the spectra have a 0.2 coherence at wavelengths of 30-40 km. Our objective for accurate strain-rate measurement is to maintain at least 0.2 coherence among the models, at a 10 km spacing, when integrated with InSAR.

2. Methods

Our InSAR/GNSS integration approach is an extension of standard published methods (e.g., *Tong et al.*, 2013; *Weiss et al.,* 2020) although in addition to secular velocity, we also calculate line-of-sight (LOS) displacement time series [e.g., *Neely et al.,* 2019]. The GNSS weekly displacements were derived by means of a median filter [*Klein et al.*, 2019] of daily time series estimated as part of a NASA MEaSUREs project [*Bock et al.*, 2016]. Moreover, we use the secular velocity from a GNSS-only interseismic model [*Zeng & Shen*, 2017] to create semi-vertical vector InSAR time series from the LOS displacements. A brief description of the method follows:

1. Gather Sentinel-1 Terrain Observations with Progressive Scans (TOPS) data from multiple tracks and re-assemble into common re-defined frames, typically 250 km by 500 km.

2. Geometrically co-register all SAR acquisitions and construct all interferograms with perpendicular baseline < 150 m and temporal separation < 90 days [*Xu et al.*, 2017; *Sandwell et al.*, 2016b].

3. Mask bodies of water and areas of persistent low coherence regions and replace them with nearest-neighbors [*Shanker & Zebker*, 2009]. This step improves the phase unwrapping accuracy which is done with Statistical-Cost, Network-Flow Algorithm for Phase Unwrapping (SNAPHU) [*Chen & Zebker*, 2002].

4. Perform elevation dependent atmospheric phase correction [*Elliott et al.*, 2008]. Compute the difference between the remaining InSAR phase and projected GNSS weekly solutions [*Klein et al.*, 2019], interpolate this difference, filter at 80-km wavelength and remove this difference from each interferogram.

5. Construct time-series using a coherence-based SBAS approach integrated with atmospheric phase correction using common-scene stacking [*Tymofyeyeva & Fialko*, 2015; *Tong & Schimdt*, 2016; *Xu et al.*, 2017].

6. Subtract a horizontal GNSS velocity model [e.g., *Zeng & Shen*, 2017] from the time-series to create semi-vertical InSAR time-series.

Since Sentinel-1 TOPS data is acquired under burst acquisition mode and there is occasional inconsistency in data coverage, especially in the early days of the mission, the frame boundaries in step 1) are a compromise between spatial coverage and acquisition numbers. The total number of interferograms generated here is 5230, connecting acquisitions from 910 dates over 9 tracks. Enhanced spectral diversity [*Prats-Iraola et al.*, 2012] is not performed in step 2, since it will remove an expected tectonic signal that will eventually supply a third InSAR component [*Li et al.,* 2021]. The estimated mis-registration could be up to 2/1000 pixel/yr along SAFS and spread across the scenes, where a constant shift from ESD is inadequate, while the performance of bivariate approach [*Wang et al.,* 2017] is yet to be evaluated. Moreover, the common scene stacking time series approach (step 5) is capable of mitigating along-track orbital errors by absorbing burst discontinuities, that are random in time, into atmospheric phase screens [*Xu et al.*, 2017]. The nearest-neighbor interpolation in step 3) is implemented so phases are allowed to vary properly along very long coastlines, and stay connected through snowy Sierras and heavy vegetations in northern California. Elevation dependency in step 4) is assumed as a bivariate quadratic polynomial thus spatial variations in atmospheric contribution are accounted for. The relatively large, 80-km wavelength filter, that is applied to the GNSS correction for each interferogram, is sufficient to absorb the large-scale atmospheric and orbital errors affecting the InSAR displacements and also accommodate areas such as the Central Valley having sparse GNSS coverage. A remove-restore approach [*Tong et al.*, 2013] using a purely horizontal secular velocity model is not used because it is incompatible with the significant vertical signal in Central Valley. Not only is this vertical deformation distributed over hundreds of kilometers, but it also has a sharp transition around the edges of the sedimentary basins. The interpolation of discrepancies between GNSS and InSAR is adopted here, taking advantage that though the vertical deformation changes dramatically over a large area, the differences from the two type of observations maybe systematic and vary slow enough in space to be well evaluated. When the final velocity is computed, the first and last four records are not used, mainly because the atmospheric correction approach gains less constraints when acquisitions are non-evenly distributed.

3. Analyses, Results and Discussions

Average Velocity

The integrated Sentinel-1 InSAR and GNSS time-series reveal a complex time-averaged velocity field (Fig. 2, 3) over the entire San Andreas fault system. The most prominent feature is the large-scale tectonic motion between the two plates with sharp transitions at creeping strike-slip faults and broader transitions at more deeply-locked faults. Superimposed on this tectonic pattern are numerous nontectonic deformations mostly related to hydrological and hydrothermal processes. These non-tectonic features are highlighted in the semi-vertical component (Fig. 2d). Our velocity maps are available as kmz files (http://topex.ucsd.edu/gmtsar/tar/San_Andreas_Xu_et_al.kmz) so that

the user can examine in detail the correlations between vertical deformation and natural and man-made surface features (See Supplementary Text S1 and Movie S1 for much more details).

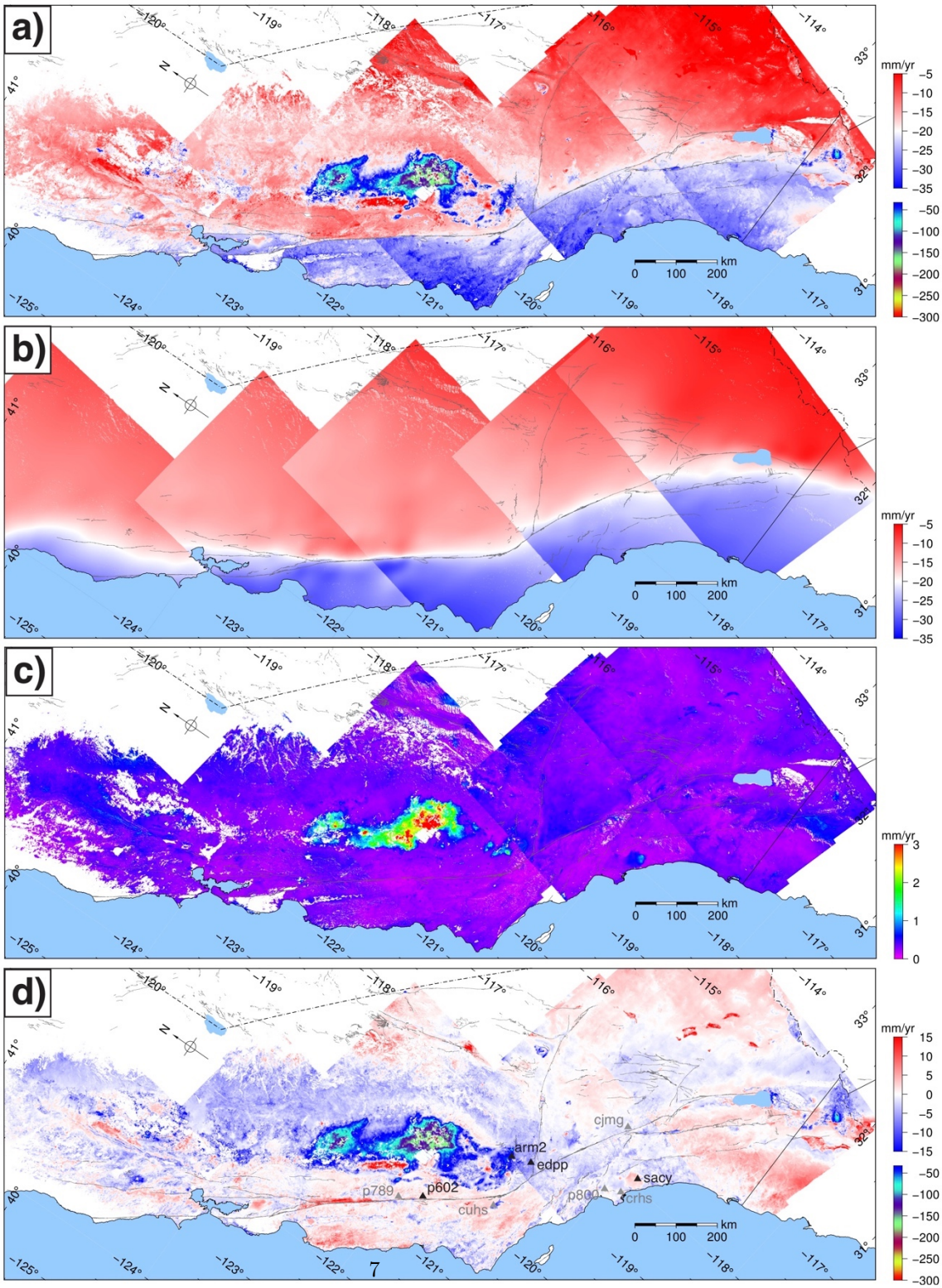
a)
b)
c)
d)
mm/yr
km
0 100 200
arm2
edpp
p602
p789
cuhs
cjmg
sacy
p800
crhs

Fig. 2. LOS deformation velocity (descending) along the San Andreas fault system. a) Total LOS deformation velocity with red color denoting motion toward the satellite and blue away from the satellite. A second color scale is added to highlight the major subsidence in the Central Valley. b) LOS velocity from *gpsgridder* [*Sandwell & Wessel*, 2016] projected into the LOS (for illustration purposes only). b) Velocity variation/uncertainty is the deviation of the time series at each pixel from a linear regression fit. The velocity discontinuities between swaths are due to the change in look angle. d) Semi-vertical velocity is the LOS with horizontal velocity model [*Zeng & Shen*, 2017] removed. The triangles in d) mark the location of GNSS stations plotted in Fig 4b (black) and Fig 4c (gray).

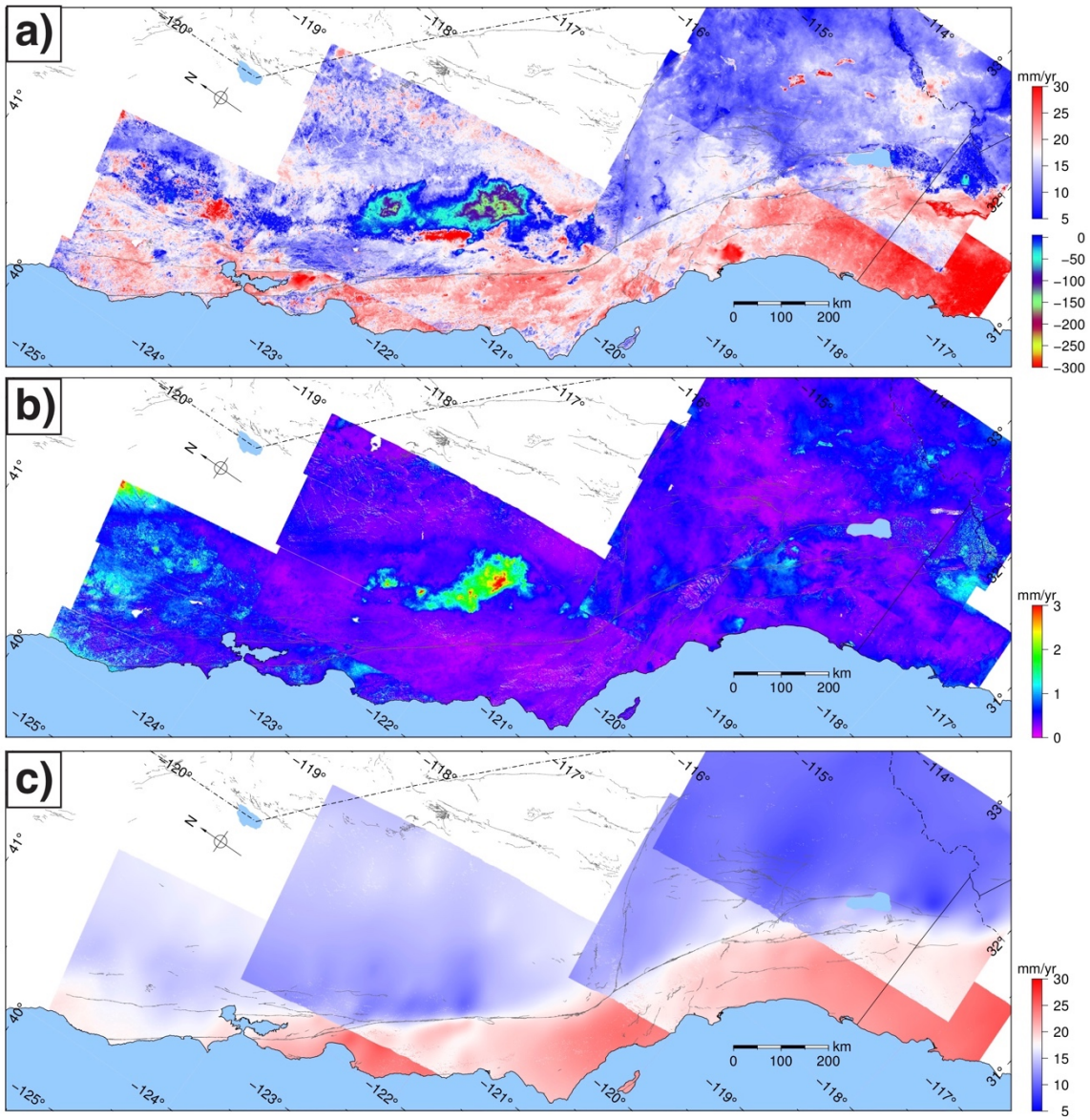

Fig. 3. LOS deformation velocity (ascending) along the San Andreas fault system. a) Total LOS deformation velocity with red color denoting motion toward the satellite and blue away from the satellite. A second color scale is added to highlight the major subsidence in the Central Valley. b) Velocity variation/uncertainty derived from linear regression on the resulting time-series. c) LOS velocity from gpsgridder [*Sandwell & Wessel*, 2016] projected into the LOS (for illustration purpose only).

LOS Time Series

We have compared the integrated InSAR/GNSS LOS time series with the GNSS-only time series and find both excellent and poor agreements (Table S2). Note the two time-series will not match exactly as our approach is essentially trusting GNSS at longer wavelengths while InSAR at short wavelengths. Fig. 4b shows several examples where there is excellent agreement between the InSAR and GNSS time-series. The typical deviation of GNSS daily solutions from its moving average is around 3-4 mm, while the integrated InSAR deviates only slightly larger, around 3-6 mm (Fig. 4a). The vertical component could largely reproduce this deviation and can be considered as the major source of discrepancy. However, there are a number of cases where the integrated InSAR GNSS time-series fail to match the GNSS solutions (Fig. 4c). In most cases this is a direct result of anomalous displacements or artifacts in the GNSS displacement time series. An extreme example is station p800 in Los Angeles showing systematic effects due to the growth of thick vegetation nearly concealing the GNSS antenna and causing a significant drift in the north direction over a period of about 2 years (overlapping with the 4.5 years of our time series) until the vegetation is cleared in May 2018 (add figure in supplement). Station CRHS also in Los Angeles and affected by vegetation and whose data after 2006 are suspect and should not be used (personal communication, Chris Walls, UNAVCO NOTA engineer) – the station was subsequently abandoned. Station CUHS in the Cuyama Valley is subject to significant subsidence of about 30 mm/yr with a seasonal signature resulting in non-tectonic horizontal displacements with amplitudes up to 30 mm. Station CJMG in the San Gabriel Mountains has annual horizontal artifacts starting in 2017 with an amplitude of 30 mm (peak to peak). Another example is station P789 on the San Andreas fault in the transition zone between locked and creeping section is experiencing uplift since 2013 of about 2.5 mm/yr but not fully sufficient to explain its misfit with InSAR. For the purpose of this study these GNSS data were not excluded. Rather, we allowed for discrepancies to exist through the integration, especially when a single station shows large mismatch, because the GNSS correction model, applied to each interferogram, is smoothed with a robust filter that down weighs the anomalous misfits. Thus, in cases a GNSS station starts to behave anomalously, the InSAR time-series remain largely unaffected (Fig. 4c). In further studies, we recommend a more conservative approach in choosing stations for the GNSS/InSAR integration. More assessment and results are available in Table S2 and Fig S1 in the supplements.

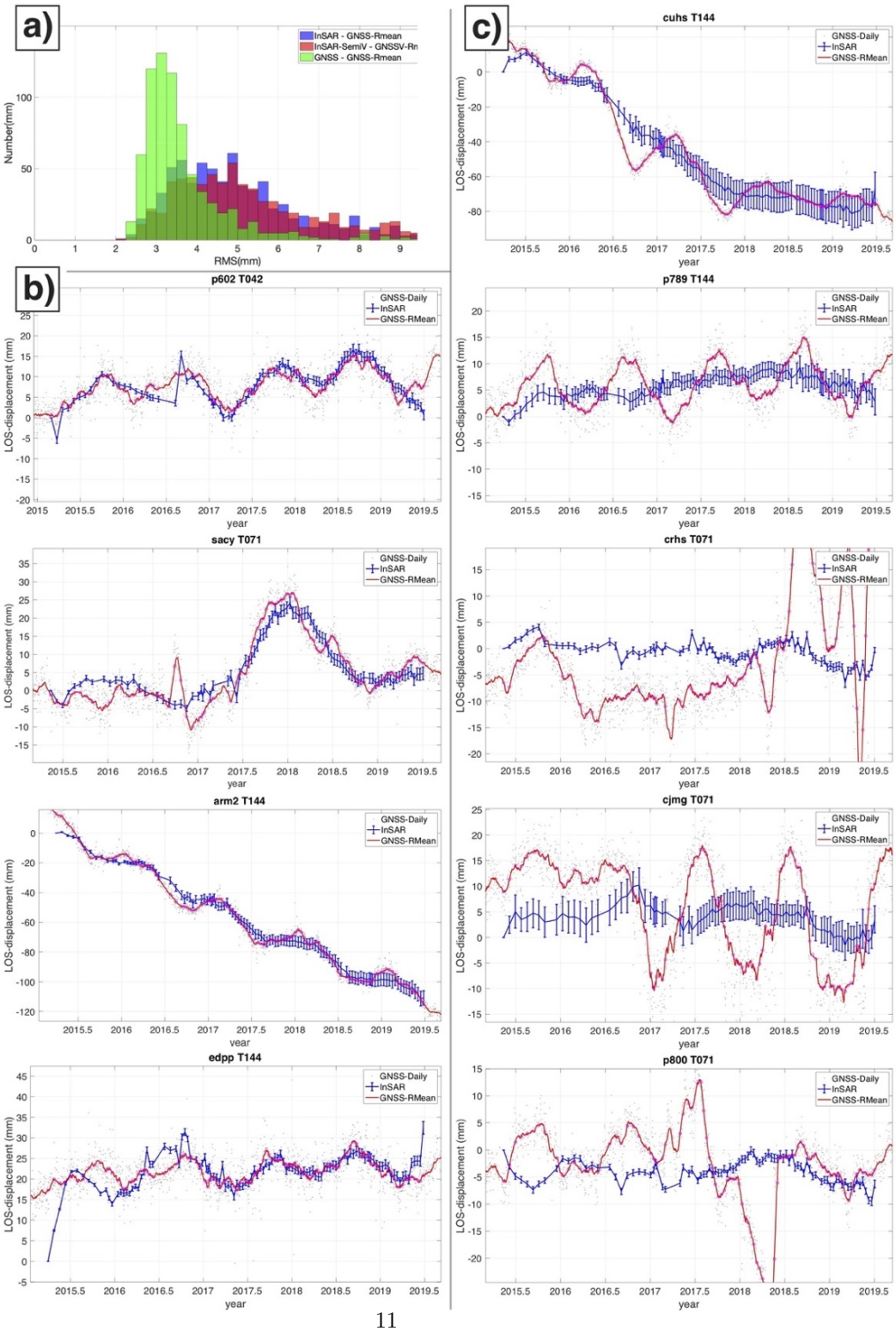
a)
InSAR - GNSS-Rmean
InSAR-SemiV - GNSSV-Rn
GNSS - GNSS-Rmean
Number(mm)
RMS(mm)
b)
p602 T042
sacy T071
arm2 T144
edpp T144
c)
cuhs T144
p789 T144
crhs T071
cjmg T071
p800 T071
GNSS-Daily
InSAR
GNSS-RMean
LOS-displacement (mm)
year

Fig. 4. Comparisons of InSAR LOS time series with GNSS time series projected into the LOS. a) Histograms of deviation from GNSS moving average (window 4 weeks). Green colors are for GNSS daily solution, blue for integrated InSAR & GNSS time-series, and red for the semi-vertical component in the integrated InSAR & GNSS time-series (horizontal GNSS model removed, comparison made with GNSS vertical component only). b) Subplots of InSAR and GNSS time series at 4 GNSS stations showing good agreement after integration. Uncertainties of InSAR time-series are standard deviations taken in 500-m boxes. c) Subplots of InSAR and GNSS time series at 5 GNSS stations showing poor agreement after integration.

Fault Creep Rate

Fault creep rate can be estimated from just two components of LOS deformation if one assumes there is no fault-normal displacement [*Xu et al.*, 2018]. By making that assumption we measure fault-parallel and vertical creep rate along each individual strand within the San Andreas Fault system (Fig. 5, Table S1). The method, which is similar to the *Bufford & Harsh* [1980] method, is to fit a linear model to the LOS data over a flat area on each side of the fault (up to 3 km) and record the offset of the linear models at the fault location. The along-fault offset locations have a typical spacing of 10 km and roughly follow the locations from the study of *Tong et al.* [2013]. Some areas of fault creep have a velocity step up to 1 km wide; In these cases, the linear fit is confined to the flatter part of the LOS data on each side of the fault (e.g., Fig. 5a, at Hayward fault). The fault creep rates estimated in this study are presented together with a compilation by *Field et al.* [2009] (Fig. 5a). Fault vertical differential (Fig. 5b) shows no systematic pattern along these faults. However, not accounting for the vertical offset will bias the horizontal offset estimates. A few larger vertical offsets (Fig 5b) are associated with subsidence at fault step-overs.

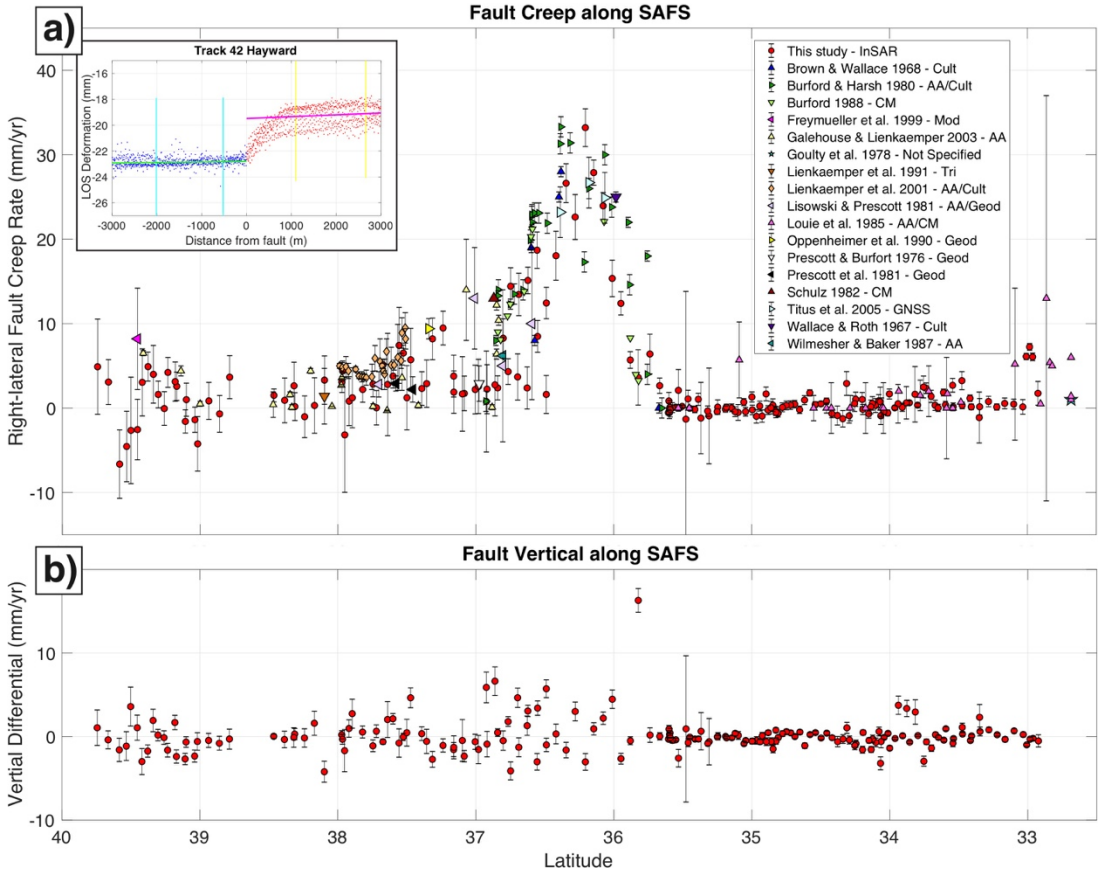

Fig. 5. Comparison of creep rate estimates along major segments of the San Andreas fault system. a) Red circles are right-lateral creep rates from decomposing two-look InSAR LOS estimates into fault parallel horizontal and vertical. Detailed estimates for each segment are available in Table S1. A compilation of creep estimates from *Field et al.* [2009] are also plotted with markers for each individual study listed in the upper right box. Survey types are listed as: AA-alignment array, CM-creep meter, Cult-cultural offset features, Geod-small geodetic array, Mod-inferred from model, Tri-trilateration. The upper left box shows an example from a descending InSAR track covering Hayward fault, showing how the estimates are performed. b) Fault vertical differential in the creep rate estimates. Positive is defined as eastern side uplift (northern side up for Garlock fault).

Velocity Decomposition

In order to compute the horizontal components of strain rate we must first construct 3 components of surface velocity (east, north and up) from only two components of LOS velocity. To accomplish this, we adopt the assumption that the direction of surface displacement matches the direction from the GNSS

velocity model [*Wright et al.*, 2004; *Tymofyeyeva & Fialko*, 2018; *Shen & Liu*, 2020]. This utilizes the local azimuth of a horizontal GNSS velocity predicted from the interseismic slip model of *Zeng & Shen* [2017] as a constraint to reduce the required degrees of freedom in the measurements from three to two. The decomposed velocity field (Fig. 6) reveals detailed spatial variations in the east-west component together with dramatic vertical motions. Some of the variations in horizontal component are associated with hydrological signals (e.g., inside Central Valley). Subsidence inside the Central Valley is greater than 30 cm/yr with other areas like Geysers, Heber and Cerro Prieto Geothermal Fields standing out in the map. Uplifts that occur at ground water recharging sites (Long Beach, Santa Clara Valley, etc.) are usually a direct reflection of human activities, some of which cannot be well represented by a single velocity (e.g., Fig 2c., GNSS station SACY). Since the velocity is derived as a linear fit, a positive rate does not necessarily result from an overall uplift. Due to the near-polar orbits, InSAR satellites are generally not very sensitive to north-south motion. Thus, the decomposed north-south component absorbs most of its information from the GNSS model, resulting in an oversmoothed field.

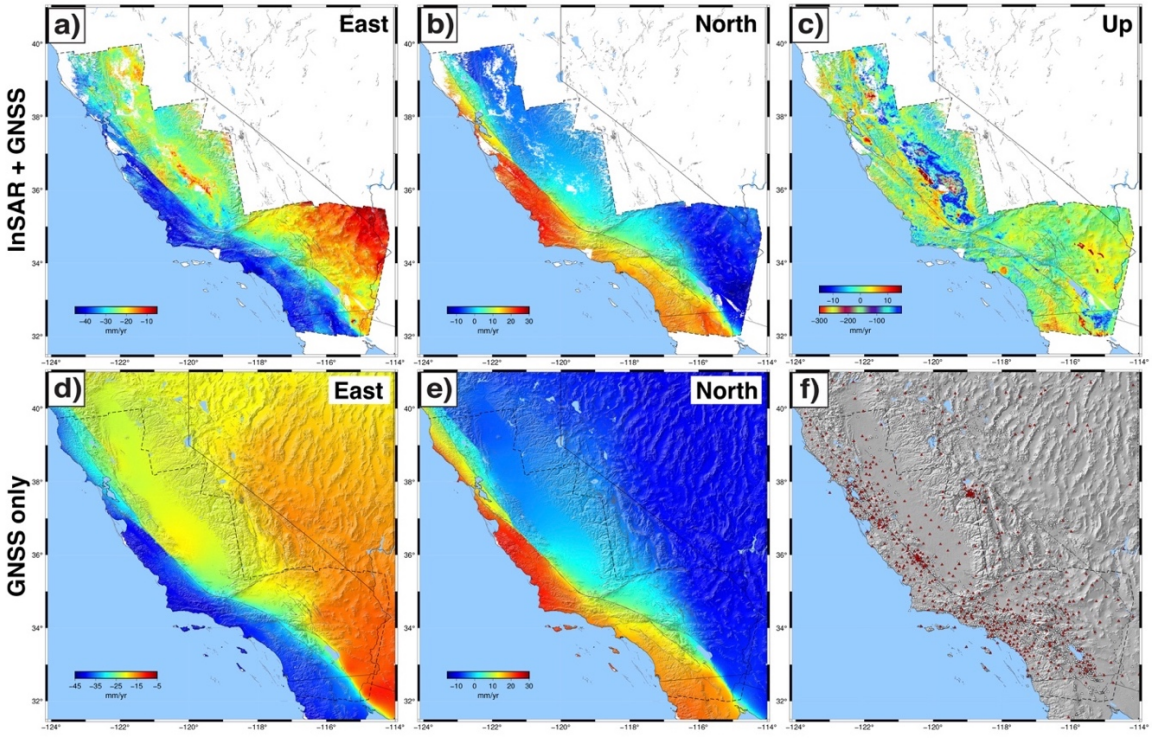

Fig 6. Surface vector velocity maps for the San Andreas fault system in the ITRF2014 coordinate system. a), b) and c) are the decomposed east, north and vertical component respectively. d) and e) are GNSS horizontal velocity model from *Zeng & Shen* [2017]. f) are stations distributions, with white trian-

gle denoting campaign sites used in the GNSS model and red triangles denoting continuous sites used both in GNSS model and InSAR/GNSS integration. Decomposition of InSAR GNSS integrated velocity maps uses information of horizontal deformation direction provided by the model shown in d) and e).

Strain Rate

The 3-D velocity maps derived from the InSAR/GNSS combination have small spatial scale variations that are associated with hydrological processes and residual atmospheric error. These models must be smoothed to extract the underlying tectonic strain rate [e.g., *Weiss et al.,* 2020]. This is accomplished by using a smoothing interpolator that has constraints from elasticity to couple the two horizontal velocity components [*Haines and Holt,* 1993] as implemented in the program *gpsgridder* in GMT [*Sandwell & Wessel*, 2016]. We first subsample both the GNSS and InSAR/GNSS horizontal velocity fields shown in Fig. 6 at a spacing of 2.5 km resulting in 40,016 2-D velocity estimates. The *gpsgridder* algorithm uses singular value decomposition of the elasticity Greens functions and we select only those associated with the largest 800 eigenvalues. We then compute the three horizontal strain rate components from the smoothed horizontal velocities. The comparison of the GNSS only and InSAR/GNSS for several components of strain rate (second invariant, maximum shear and dilatation) are shown in Fig 7.

The San Andreas fault is well delineated by the concentrated high-strain ($>$ 200 nanostrain/yr). Compared to the prediction of the GNSS-only strain rate model, the integrated InSAR/GNSS model reveals larger strain concentration, especially at locations where there is known surface creep (e.g., creeping section of SAFS and Hayward fault). Maacama and Bartlett Springs both have much larger strain concentrations in the InSAR/GNSS model although this may be a consequence of the assumption that the InSAR deformation is parallel to the GNSS deformation. Dilatational strain predicted by the integrated InSAR/GNSS model shows extension in the Central Valley associated with the subsidence from groundwater extraction. The shear component is also larger in areas of known hydrological signals. There is a prominent shear strain anomaly in the InSAR/GNSS strain rate maps (Fig. 7e, f) that is to the east of and parallel to the creeping section. However, there is not enough GNSS data in the region to determine if this is a real strain-rate anomaly or artifact from the interpolation approach. Overall, the strain is more widely distributed in the integrated InSAR/GNSS model, with significant components being off-fault. The remaining questions are how much of these are from tectonic motion and how much from hydrological activities, and whether these off-fault components are steady over time or just transients. Answering these will be the key leading to accurate assessment of the strain/moment accumulation and the associated seismic hazards.

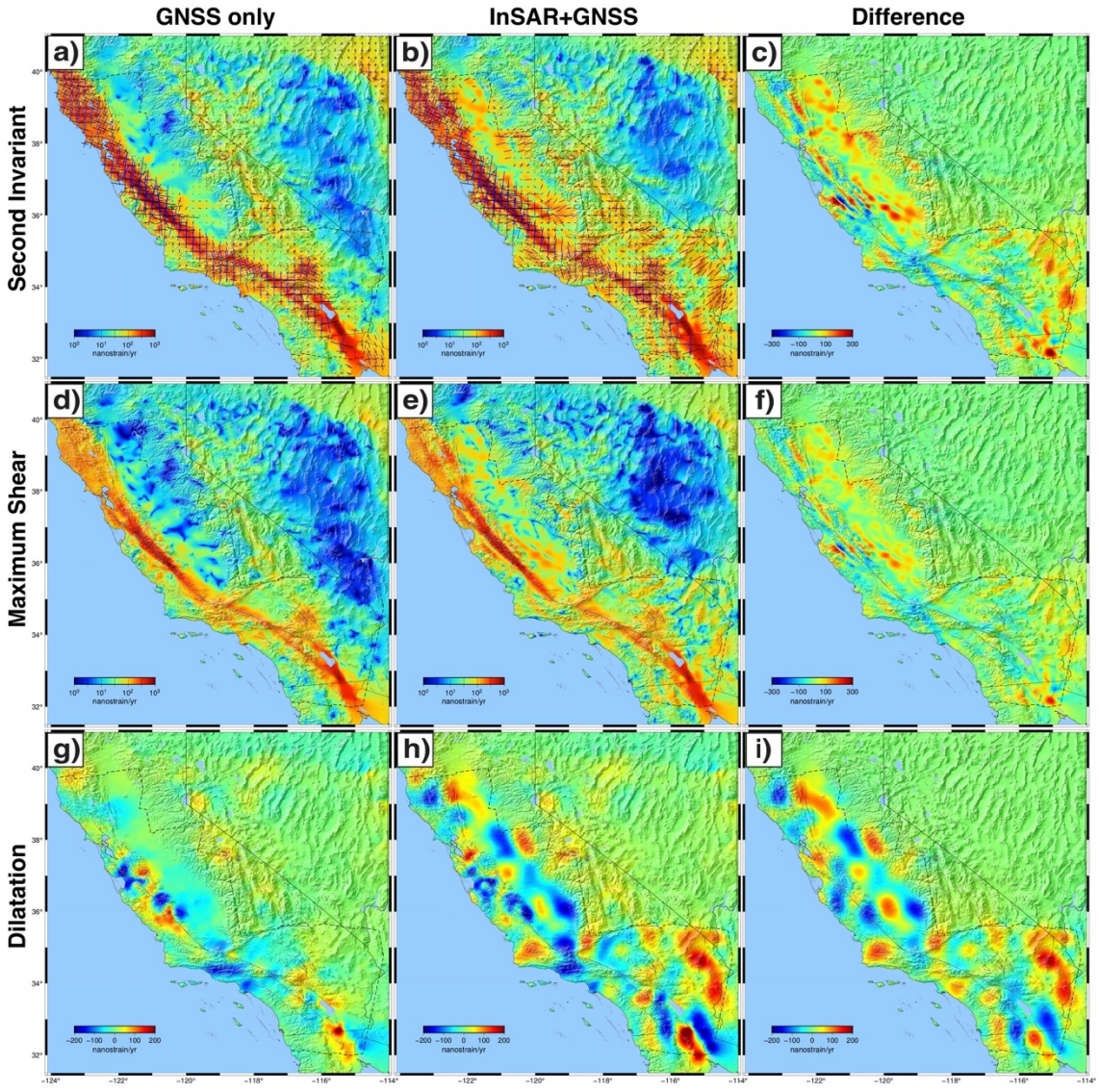

Fig. 7. Strain rate maps for San Andreas fault system. a) is the second invariant of strain rate derived with gpsgridder using GNSS data only. Black and blue bars represent compressional and extensional principal strain rates respectively, and they are clipped at 100 nanostrain/yr. b) is same as a) but using decomposed InSAR+GNSS horizontal velocity components. c) Differences between a) and b). d) and e) Maximum shear strain rate (defined as $\max\left(\dot{\varepsilon}_1 - \dot{\varepsilon}_2\right)/2$, *Savage et al.,* 2001) maps with f) being their difference. g) and h) Dilatation rate (defined as $(\dot{\varepsilon}_1 + \dot{\varepsilon}_2)$, *Savage et al.,* 2001) with i) being their difference. In all plots, the dashed bounding box denotes the area with Sentinel-1 coverage from two look

directions.

5. Conclusion

The main conclusions are:

- Current strain rate models based only on point GNSS measurements are reliable at longer wavelengths (> 30-40 km) but have large differences at shorter wavelengths so they cannot achieve the 100 nanostrain/yr accuracy threshold for assessing seismic hazard. In addition, there are significant transient deformation processes (e.g., hydrologic, magmatic, and tectonic) having strain rate signals that exceed the 100 nanostrain/yr threshold needed for hazard assessment.
- We developed an approach to integrate Sentinel-1 InSAR and GNSS time-series (4.5 years) over the entire San Andreas fault system from the ascending and descending look directions. This analysis was enabled by the frequent, high-quality, observations from the Sentinel-1 satellites.
- A video tour of the high-resolution LOS velocity maps reveals a wide array of deformation processes including: active faults and stepovers; extraction and recharge of groundwater, petroleum and geothermal fluids; and continuous expansion of the surface of dry lake beds (Movie S1, and available at https://www.youtube.com/watch?v=SxNLQKmHWpY).
- The two components of average LOS velocity are used to refine and update estimates of creep rate along the major strands of the San Andreas fault system.
- The two LOS components are decomposed into 3-components of velocity by assuming the direction of deformation matches those predicted by a GNSS-only velocity model.
- The higher spatial resolution vector velocity maps are used to estimate the three components of horizontal crustal strain rate. The results show significant off-fault strain, yet challenges remain in separating the contribution from tectonic and hydrologic sources and whether hydrologic strain will increase seismic hazards.
- Given the 20-year plus observation plan of the twin Sentinel-1 satellites, as well as continued GNSS operations, these high spatial resolution, time-dependent products will continue to improve.

Acknowledgements

The authors want to thank European Space Agency for the extraordinary

data open policy on the Sentinel-1 mission and want to thank Alaska Satellite Facility and UNAVCO for archiving the data and the precise orbital products. This study was funded by the NASA Earth Surface and Interior Program (80NSSC19K1043 and NNX17AD99G), the NASA MEaSUREs Program (NNH17ZDA001N), the National Science Foundation, Office of Advanced Cyberinfrastructure (OAC-1834807), and the Southern California Earthquake Center (SCEC) (20074). SCEC is funded by the NSF cooperative Agreement EAR-1033462 and USGS Cooperative Agreement G12AC20038. All data are originally available through Sentinel Scientific Data Hub (https://scihub.copernicus.eu) and Alaska Data Search Vertex (https://search.asf.alaska.edu). Processed data are currently available at https://topex.ucsd.edu/gmtsar/insargen and on the move to SCEC as part of the Community Geodetic Model (https://www.scec.org/research/cgm).

References

Shanker, A. P., & Zebker, H. A. (2009). Sparse two-dimensional phase unwrapping using regular grid methods. *IEEE Geoscience and Remote Sensing Letters*, *6*(3), 519-522.

Bayona, J.A., Savran, W., Strader, A., Hainzl, S., Cotton, F. and Schorlemmer, D., 2021. Two global ensemble seismicity models obtained from the combination of interseismic strain measurements and earthquake-catalogue information. *Geophysical Journal International*, 224(3), pp.1945-1955.

Bock, Y., S. Kedar, A. W. Moore, P. Fang, J. Geng, Z. Liu, D. Melgar, S. E. Owen, M. B. Squibb, F. Webb (2016), Twenty-Two Years of Combined GPS Products for Geophysical Applications and a Decade of Seismogeodesy, International Association of Geodesy Symposia, Springer International Publishing, doi:10.1007/1345_2016_220.

Burford, R. O., & Harsh, P. W. (1980). Slip on the San Andreas fault in central California from alinement array surveys. *Bulletin of the Seismological Society of America*, *70*(4), 1233-1261.

Chen, C. W., & Zebker, H. A. (2002). Phase unwrapping for large SAR interferograms: Statistical segmentation and generalized network models. *IEEE Transactions on Geoscience and Remote Sensing*, 40(8), 1709-1719.

Elliott, J. R., Biggs, J., Parsons, B., & Wright, T. J. (2008). InSAR slip rate determination on the Altyn Tagh Fault, northern Tibet, in the presence of topographically correlated atmospheric delays. *Geophysical Research Letters*, *35*(12).

Elliott, J.R., Walters, R.J. and Wright, T.J., 2016. The role of space-based observation in understanding and responding to active tectonics and earthquakes. *Nature Communications*, 7, p.13844.

Emardson, T. R., et al. (2003), Neutral atmospheric delay in interferometric synthetic aperture radar applications: Statistical description and mitigation, *Journal of Geophysical Research-Solid Earth*, 108(B5).

Field, E. H., Dawson, T. E., Felzer, K. R., Frankel, A. D., Gupta, V., Jordan, T. H., ... & Wills, C. J. (2009). Uniform California earthquake rupture forecast, version 2 (UCERF 2). *Bulletin of the Seismological Society of America*, *99*(4), 2053-2107.

Field, E. H., Arrowsmith, R. J., Biasi, G. P., Bird, P., Dawson, T. E., Felzer, K. R., ... & Zeng, Y. (2014). Uniform California Earthquake Rupture Forecast, Version 3 (UCERF3)—The Time-Independent Model. *Bulletin of the Seismological Society of America*, 104(3), 1122-1180.

Field, E.H., Biasi, G.P., Bird, P., Dawson, T.E., Felzer, K.R., Jackson, D.D., Johnson, K.M., Jordan, T.H., Madden, C., Michael, A.J. and Milner, K.R., 2015. Long-term time-dependent probabilities for the third Uniform California Earthquake Rupture Forecast (UCERF3). *Bulletin of the Seismological Society of America*, 105(2A), pp.511-543.

Flesch, L. M., Holt, W. E., Haines, A. J., & Shen-Tu, B. (2000). Dynamics of the Pacific-North American plate boundary in the western United States. *Science*, 287(5454), 834-836.

Hackl, M., R. Malservaisi, and S. Wdowinski (2009), Strain pattern from dense GPS networks, *Nat. Hazards Earth Syst.*, 9., 1177-1187.

Haines, A.J. and Holt, W.E., 1993. A procedure for obtaining the complete horizontal motions within zones of distributed deformation from the inversion of strain rate data. *Journal of Geophysical Research: Solid Earth*, 98(B7), pp.12057-12082.

Holt, W. E., & Shcherbenko, G. (2013). Toward a continuous monitoring of the horizontal displacement gradient tensor field in Southern California using cGPS observations from Plate Boundary Observatory (PBO). *Seismological Research Letters*, *84*(3), 455-467.

Klein, E., Bock, Y., Xu, X., Sandwell, D. T., Golriz, D., Fang, P., & Su, L. (2019). Transient deformation in California from two decades of GPS displacements: Implications for a three-dimensional kinematic reference frame. *Journal of Geophysical Research: Solid Earth*, *124*(11), 12189-12223.

Kreemer, C., Blewitt, G., & Klein, E. C. (2014). A geodetic plate motion and global strain rate model. *Geochemistry, Geophysics, Geosystems*, 15(10), 3849-3889.

Li, X., Jónsson, S., & Cao, Y. (2021). Interseismic deformation from Sentinel-1 burst-overlap interferometry: Application to the southern Dead Sea fault. *In review for GRL*

Loveless, J. P., and B. J. Meade (2011), Stress modulation on the San Andreas fault by interseismic fault system interactions, *Geology*, 39(11), 1035-1038.

McCaffrey, R. (2005), Block kinematics of the Pacific–North America plate boundary in the southwestern United States from inversion of

GPS, seismological, and geologic data, *J. Geophys. Res.*, 110, B07401, doi:10.1029/2004JB003307.

Neely, W. R., Borsa, A. A., & Silverii, F. (2019). GInSAR: A cGPS correction for enhanced InSAR time series. *IEEE Transactions on Geoscience and Remote Sensing*, *58*(1), 136-146.

Parsons, T. (2006), Tectonic stressing in California modeled from GPS observations, *J. Geophys. Res.* 111, doi:10.1029/2005JB003946.

Parsons, T., Johnson, K. M., Bird, P., Bormann, J., Dawson, T. E., Field, E. H., ... & Zeng, Y. (2013). Appendix C—Deformation models for UCERF3.

Petersen, M. D., Y. Zeng, K. M. Haller, R. McCaffrey, W. C. Hammond, P. Bird, M. Moschetti, Z. Shen, J. Bormann, and W. Thatcher [2014] Geodesy- and geology-based slip-rate models for the Western United States (excluding California) national seismic hazard maps, U.S. Geol. Surv. Open-File Rep., 2013-1293, 38 pages doi.org/10.3133/ofr20131293.

Platt J. P. and T. W. Becker (2010), Where is the real transform boundary in California?, *Geochem. Geophys. Geosyst.*, 11, Q06012, doi:10.1029/2010GC003060.

Prats-Iraola, P., Scheiber, R., Marotti, L., Wollstadt, S., & Reigber, A. (2012). TOPS interferometry with TerraSAR-X. *IEEE Transactions on geoscience and remote sensing*, *50*(8), 3179-3188.

Rollins, C., Wright, T.J., Weiss, J.R., Hooper, A.J., Walters, R.J., Lazecky, M., Morishita, Y. and Maghsoudi, Y., 2020, December. Tectonic strain rates across the central Alpine-Himalayan Belt from Sentinel-1 InSAR and GNSS observations, and implications for seismic hazard. In AGU Fall Meeting 2020. AGU.

Savage, J. C., Gan, W., & Svarc, J. L. (2001). Strain accumulation and rotation in the Eastern California Shear Zone. *Journal of Geophysical Research: Solid Earth*, *106*(B10), 21995-22007.

Sandwell, D.T. and Wessel, P., (2016). Interpolation of 2-D vector data using constraints from elasticity. *Geophysical Research Letters*, 43(20).

Sandwell, D.T., Zeng, Y., Shen, Z.K., Crowell, B., Murray, J., McCaffrey, R. and Xu, X., (2016a). The SCEC community geodetic model V1: Horizontal velocity grid. In SCEC Annu. Meeting.

Sandwell D. T. Xu X. Mellors R. Wei M. Tong X., and Wessel P. (2016b). GMTSAR: An InSAR Processing System Based on Generic Mapping Tools, Second Ed., available at http://topex.ucsd.edu/gmtsar/tar/GMTSAR_2ND_TEX.pdf (last accessed December 2019).

Shen, Z.K. and Liu, Z., 2020. Integration of GPS and InSAR Data for Resolving 3-Dimensional Crustal Deformation. *Earth and Space Science*, 7(4), e2019EA001036.

Shen, Z. K., Wang, M., Zeng, Y., & Wang, F. (2015). Optimal interpolation of spatially discretized geodetic data. *Bulletin of the Seismological Society of America*, 105, 2117-2127.

Smith-Konter, B., & Sandwell, D. (2009). Stress evolution of the San Andreas fault system: Recurrence interval versus locking depth. *Geophysical Research Letters*, *36*(13).

Tape, C., P. Muse, M. Simons (2009), D. Dong, and F. Webb, Multiscale estimation of GPS velocity fields, *Geophys. J. Int.*, 179, 945-971.

Tong, X., D. Sandwell, and B. Smith-Konter (2013), High-resolution interseismic velocity data along the San Andreas Fault from GPS and InSAR, *J. Geophys. Res. Solid Earth*, 118, doi:10.1029/2012JB009442.

Tong, X., B. Smith-Konter, and D. T. Sandwell (2014), Is there a discrepancy between geological and geodetic slip rates along the San Andreas Fault System?, *J. Geophys. Res. Solid Earth*, 119, doi:10.1002/2013JB010765.

Tong, X., & Schmidt, D. (2016). Active movement of the Cascade landslide complex in Washington from a coherence-based InSAR time series method. *Remote Sensing of Environment*, *186*, 405-415.

Tymofyeyeva, E., & Fialko, Y. (2015). Mitigation of atmospheric phase delays in InSAR data, with application to the Eastern California Shear Zone. *Journal of Geophysical Research: Solid Earth*, 120(8), 5952-5963.

Tymofyeyeva, E., & Fialko, Y. (2018). Geodetic evidence for a blind fault segment at the southern end of the San Jacinto Fault Zone. *Journal of Geophysical Research: Solid Earth*, 123, 878–891. https://doi.org/10.1002/2017JB014477.

Uieda, L. (2018). Verde: Processing and gridding spatial data using Green's functions. *Journal of Open Source Software*, *3*(30), 957.

Wang, K., Xu, X., & Fialko, Y. (2017). Improving burst alignment in TOPS interferometry with bivariate enhanced spectral diversity. *IEEE Geoscience and Remote Sensing Letters*, *14*(12), 2423-2427.

Wei, M., D. T. Sandwell, and B. Smith-Konter (2010), Optimal combination of InSAR and GPS for measuring interseismic crustal deformation, *J. Adv. in Space Res.*, doi: 10.1016/j.asr.2010.03.013.

Weiss, J. R., Walters, R. J., Morishita, Y., Wright, T. J., Lazecky, M., Wang, H., ... & Parsons, B. (2020). High-resolution surface velocities and strain for Anatolia from Sentinel-1 InSAR and GNSS data. *Geophysical Research Letters*, *47*(17), e2020GL087376.

Wessel, P., Luis, J. F., Uieda, L., Scharroo, R., Wobbe, F., Smith, W. H. F., & Tian, D. (2019). The generic mapping tools version 6. *Geochemistry, Geophysics, Geosystems*, *20*(11), 5556-5564.

Wright, T. J., Parsons, B. E., & Lu, Z. (2004). Toward mapping surface deformation in three dimensions using InSAR. *Geophysical Research Letters*, 31(1).

Xu, X., Sandwell, D. T., Tymofyeyeva, E., González-Ortega, A., & Tong, X. (2017). Tectonic and anthropogenic deformation at the Cerro Prieto geothermal step-over revealed by Sentinel-1A InSAR. *IEEE Transactions on Geoscience and Remote Sensing*, 55(9), 5284-5292.

Xu, X., Ward, L. A., Jiang, J., Smith-Konter, B., Tymofyeyeva, E., Lindsey, E. O., ... & Sandwell, D. T. (2018). Surface creep rate of the southern San Andreas fault modulated by stress perturbations from nearby large events. *Geophysical Research Letters*, *45*(19), 10-259.

Zeng Y. and Z.-K. Shen (2016). A Fault-Based Model for Crustal Deformation, Fault Slip Rates and Off-Fault Strain Rate in California, *Bulletin of the Seismological Society of America*,, 106(2), doi:10.1785/0120140250.

Zeng, Y., & Shen, Z. K. (2017). A Fault-Based Model for Crustal Deformation in the Western United States Based on a Combined Inversion of GPS and Geologic Inputs. *Bulletin of the Seismological Society of America*, *107*(6), 2597-2612.

Zeng, Y., Petersen, M. D., & Shen, Z.-K. (2018). Earthquake potential in California-Nevada implied by correlation of strain rate and seismicity. *Geophysical Research Letters*, 45, 1778–1785. https://doi.org/10.1002/ 2017GL075967